RSC Advances

PAPER

View Article Online
View Journal | View Issue

Cite this: *RSC Adv.*, 2020, **10**, 12432

Strain-induced structural phase transition, electric polarization and unusual electric properties in photovoltaic materials $CsMI_3$ (M = Pb, Sn)†

Xiao-Rong Cheng,‡[a] Xiao-Yu Kuang,‡[a] Hao Cheng,[a] Hao Tian,*[bc] Si-Min Yang,[a] Miao Yu,[a] Xi-Long Dou[a] and Ai-Jie Mao*[a]

Received 21st December 2019
Accepted 18th March 2020

DOI: 10.1039/c9ra10791f

rsc.li/rsc-advances

The structural phase transition, ferroelectric polarization, and electric properties have been investigated for photovoltaic films $CsMI_3$ (M = Pb, Sn) epitaxially grown along (001) direction based on the density functional theory. The calculated results indicate that the phase diagrams of two epitaxial $CsPbI_3$ and $CsSnI_3$ films are almost identical, except critical transition strains varying slightly. The epitaxial tensile strains induce two ferroelectric phases $Pmc2_1$, and $Pmn2_1$, while the compressive strains drive two paraelectric phases $P2_12_12_1$, $P2_12_12$. The larger compressive strain enhances the ferroelectric instability in these two films, eventually rendering them another ferroelectric state *Pc*. Whether $CsPbI_3$ or $CsSnI_3$, the total polarization of $Pmn2_1$ phase comes from the main contribution of B-position cations (Pb or Sn), whereas, for $Pmc2_1$ phase, the main contributor is the I ion. Moreover, the epitaxial strain effects on antiferrodistortive vector, polarization and band gap of $CsMI_3$ (M = Pb, Sn) are further discussed. Unusual electronic properties under epitaxial strains are also revealed and interpreted.

1 Introduction

Due to the improvement of public environmental awareness in recent years, the direct conversion of solar energy into electricity has attracted great attention.[1,2] Organic–inorganic halide is a photoelectric conversion material, which is mainly used in dye-sensitized solar cells (DSCs) because it costs less and the raw materials are abundant, especially this $CH_3NH_3PbI_3$ materials.[3–6] In decades, the photovoltaic efficiency has reached nearly 20% for $CH_3NH_3PbI_3$ materials, but practicability needs to improve on account of the volatile and thermodynamically unstable nature of organic molecules.[7,8] Recently, a stable hexagonal phase with the face sharing PbI_6 octahedra rather than the corner-connected octahedra of $CH_3NH_3PbI_3$ has been reported based on the first-principles calculations.[9] While all-inorganic halides not only made up for the thermodynamically unstable characteristics of organic molecules but also maintained a high photovoltaic efficiency.[10–12] Numerous studies indicate the most ideal photovoltaic materials possess about 1.4 eV band gap.[13,14] $CsSnI_3$ (CSI) materials have band gap of about 1.3 eV at room temperature.[15–18] On the other hand, the band gap values of $CsPbI_3$ (CPI) materials are ranging from 1.75 eV to 2.13 eV, which further reveals that $CsMI_3$ (M = Pb, Sn) are potential candidates for photovoltaic materials.[19]

Unfortunately, $CsMI_3$ (M = Pb, Sn) have phase instability in the ambient environment. One the one hand, the CSI will appear *Pnma*, $Pm\bar{3}m$, *P4/mbm* phase separately when the temperature changes.[16,20,21] On the other hand, although α-$CsPbI_3$ is the ideal photovoltaic material for CPI,[11,22] it can easily form other structures.[11,23–25] Moreover, $CsMI_3$ (M = Pb, Sn) have ferroelectric instability.[18]

Despite shortcomings, $CsMI_3$ (M = Pb, Sn) have their own advantages. For CSI, firstly, the effective mass of the small pores directly results in good conductivity, high hole mobility and large energy.[26,27] It is found that the black orthorhombic phase (*Pnma*) of CSI has one of the highest observed hole mobility in the p-type semiconductor with a direct band gap.[28] Besides, Sn atom replaces toxic Pb atoms, which can be achieved with an excellent photovoltaic efficiency[2,20] and more conducive to the commercial application of photovoltaic materials for the future.[29,30] However, the phase instability of CSI is a critical hurdle in practical application. On the bright side, the experimentally synthesized CSI nanowires[31] had a great commercial application with the controllable growth direction and size. And a novel stain-mediated phase stabilization strategy is demonstrated to significantly enhance the phase stability of cubic α-$CsPbI_3$ phase.[32] Thus, CPI as a photovoltaic efficiency material, the biggest advantage is more stable and efficient.[23,33–39] In

[a]*Institute of Atomic and Molecular Physics, Sichuan University, Chengdu 610065, China. E-mail: scu_mij@126.com*

[b]*National Laboratory of Solid State Microstructures and Collaborative Innovation Center of Advanced Microstructures, Department of Materials Science and Engineering, Nanjing University, Nanjing 210093, China. E-mail: tiao2007@126.com*

[c]*Jiangsu Key Laboratory of Artificial Functional Materials, Nanjing University, Nanjing 210093, China*

† Electronic supplementary information (ESI) available. See DOI: 10.1039/c9ra10791f

‡ Authors contributed equally to this work.

addition, quantum dots of CPI[38] produced nearly 100% photoluminescence quantum yield. Furthermore, ferroelectric material can achieve good photovoltaic efficiency.[40,41] As we all know, $CsMI_3$ (M = Pb, Sn) are good photovoltaic materials and have ferroelectric performance,[11,18,20,26,42] such as the $BiFeO_3$, $EuTiO_3$, $BaTiO_3$ and $PbTiO_3$ materials.[27,40,43–45]

Besides, through the study of Sn and Pb halides, we found that strain or pressure can change the band gap value,[46,47] which can improve the absorption effect of photovoltaic materials and enhance the conversion efficiency. Hence, we adopted the misfit strain (tensile and compressive strain) method to realize the phase transition and search the suitable band gap of $CsMI_3$ (M = Pb, Sn) halides to photovoltaic materials. The main purpose was to explore the possible phases of the (001) direction halide perovskite films. It is worth noting that two paraelectric phases $P2_12_12_1$, $P2_12_12$ and one polarization phase *Pc* are found under compressive strain, which was rarely studied in perovskite films previously.

2 Computational details

The electronic structures and properties of the $CsMI_3$ (M = Pb, Sn) are investigated based on the density-functional theory (DFT) as implemented in the Vienna *Ab initio* Simulation Package (VASP).[48] The exchange and correlation functional PBEsol[49] implemented the generalized gradient approximation (GGA) method[50] is employed in the whole calculation. The 550 eV as the plane wave energy cutoff and $6 \times 6 \times 4$ *k*-points in the irreducible Brillouin zone are applied to relax fully all structures in this paper. The energy convergence criterion is 10^{-6} eV, and force criterion convergence in the structural optimization is 0.001 eV $Å^{-1}$. For (001) epitaxial films, we control the lattice constants $a_1(=\sqrt{2}\,a_{IP})$ and $a_2(=\sqrt{2}\,a_{IP})$ in the plane, and optimize the lattice constant a_3 $(=2a_{IP}+\delta)$ in the (001) direction. Hence, the lattice parameters a_1, a_2, a_3 are directed along pseudocubic [110], [$\bar{1}$10] and [001]. Correspondingly, The misfit strain is defined as $(a - a_0)/a_0$ in our work. Then, two different methods are employed to estimate the electric polarization, one is Berry Phase method[51] contained ionic and electronic polarization contribution, the other is Born effective charges with the atomic displacements:[52]

$$P = \frac{e}{V}\sum_{\alpha\beta} Z^{*i}_{\alpha\beta}\mu^{i}_{\beta} \quad (1)$$

Moreover, the space groups of these equilibrium phases are defined by the FINDSYM program.[53] The crystal structures are drawn by the VESTA software.[54] The phonon dispersion curve of a $2 \times 2 \times 2$ cubic supercell is calculated by Phonopy with density functional perturbation theory (DFPT).[55,56]

3 Results and discussion

3.1 Structural phase transitions

As we all know, the rich structural phases of perovskite-type compounds can trace back to the phonon instability of highly symmetric cubic structure (with $Pm\bar{3}m$ space group). Fig. S1(a)† reveal that unstable phonon modes at different high-symmetric *Q* points in the ideal cubic structure of $CsPbI_3$, as evidenced by, *e.g.*, gamma point (corresponding to ferroelectric instability), *M* point (associated with in-phase antiferrodistortive instability), and *R* point (related to anti-phase antiferrodistortive instability). How does the epitaxial strain effect these phonon instabilities? Which instability will possess the larger imaginary frequency and further play a leading role in structural transitions? Let us firstly start from the strain-dependent frequencies in $CsPbI_3$, as shown in Fig. S1(b)†. The imaginary frequency of gamma point increases rapidly comparing with that of other points under lager compressive and tensile strains, which reveals the possibility of strain-driven ferroelectric phase transitions.

Based on this possibility, for $CsMI_3$ (M = Pb, Sn) films in epitaxial (001) direction, the rich phase diagram has been investigated using first-principles calculation by taking compressive and tensile strains into consideration. In our investigation, a series of structural phases (such as *Pbnm*, *I*4/*mcm*, $Pmc2_1$, $Pmn2_1$, $Pna2_1$, *Pc* and so on.) are considered to obtain the stable structures under strain effect. In order to prove the reliability and effectiveness of our calculations, the total energy and axial ratio of the most stable phases *vs.* misfit strains are plotted in Fig. 1 for epitaxial (001) CPI and CSI thin films, enriching the phase diagram of CSI film in the epitaxial [001] direction reported previously.[57] Fig. 1 shows that the phase diagrams of $CsMI_3$ (M = Pb, Sn) are basically the same, except the different misfit strain values of the same phase. Moreover, the total energy of all the phases contained metastable phases *vs.* misfit strains are presented in Fig. S2† for epitaxial (001) CPI

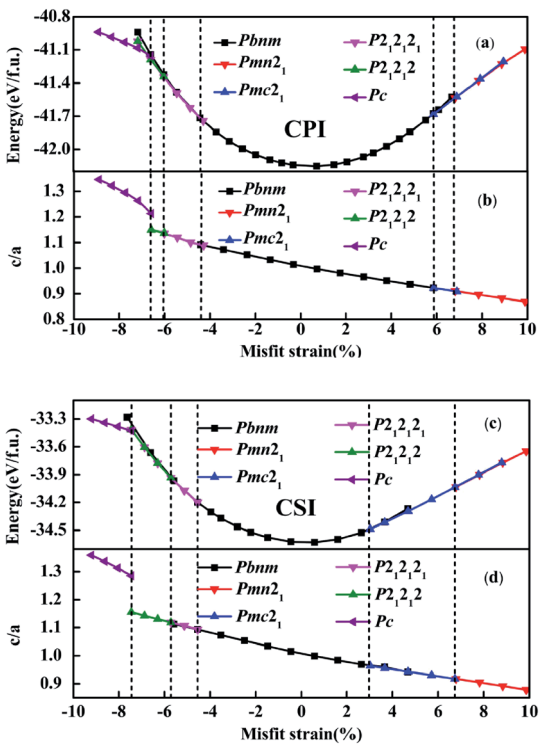

Fig. 1 The total energy and axial ratio *vs.* misfit strain in the [001] epitaxial CPI and CSI thin films.

and CSI thin films. Fig. 1 and S2† show that our calculated results are not consistent with the report previously for CSI,[57] especially in the compressive strain region. Herein, except for the structural phases *Pbnm*, *P*4*bm*, *P*4/*mbm* and $Pmc2_1$ reported by ref. 57–59, several stable phases are found under different misfit strains. Hence, six equilibrium states *Pc*, $P2_12_12_1$, $P2_12_12$, *Pbnm*, $Pmc2_1$, and $Pmn2_1$ for CPI (so do CSI) can be obtained, respectively. Correspondingly, the structural diagram of the most stable phases (*Pc*, $P2_12_12$, $P2_12_12_1$, *Pbnm*, $Pmc2_1$, $Pmn2_1$) are presented in Fig. S3.† In all calculations, the misfit strains are calculated as $\eta = (a - a_0)/a_0$, then we can get different η by adjusting a. The lattice parameter $a_0 = 8.59$ Å of ground state *Pbnm* for CSI is in good agreement with the previous experimental results.[28] The paraelectric phase *Pbnm* can be described by $a^-a^-c^+$ tilting pattern, and the in-plane component of $AAFD_{xy}$ (antiphase antiferrodistortive) vector is about 8.89° for CPI (6.71° for CSI) and out-of-plane component of the $IAFD_z$ (in-phase antiferrodistortive) vector is about 12.56° (10.76° for CSI) seen from Fig. 2.

In the tensile strain region, our results are almost the same with previous results except for different misfit strain values for CSI.[57] Whether CPI or CSI film, the stable phases *Pbnm*, $Pmc2_1$ and $Pmn2_1$ have been obtained under the epitaxial strain region. When the misfit strain varies from 0 to 5.85% for CPI and from 0 to 3.01% for CSI, the phase is still *Pbnm*. At misfit strain 5.85% and 3.01%, a phase transition has happened from *Pbnm* to $Pmc2_1$ for CPI and CSI, respectively. The $Pmc2_1$ phase is still retained with the misfit strain ranging from 5.85% to 6.89% for CPI, and from 3.01% to 6.74% for CSI, which can be described by $a^-a^-c^+$ tilting pattern. When the misfit strains reach to 6.89% and 6.74%, a new phase $Pmn2_1$ is found for CPI and CSI, respectively. $Pmn2_1$ phase with $a^-a^-c^+$ tilting pattern would be retained when the tensile strain increases.

In the compressive strain region, the biggest difference between our calculated results and the previous results is that the phases ($P2_12_12$, $P2_12_12_1$, *Pc*) are found, but *P*4*bm* and *P*4/*mbm* reported previously do not appear.[57] From Fig. S2† (seen in SM), one can see that whether *P*4*bm* or *P*4/*mbm* has higher energy than $P2_12_12$, $P2_12_12_1$ or *Pc* at the corresponding strain values. When $-4.42\% < \eta < 0$ for CPI ($-4.55\% < \eta < 0$ for CSI), the ground state is always *Pbnm* state. When $-6.01\% < \eta < -4.42\%$ for CPI ($-5.71\% < \eta < -4.55\%$ for CSI), a new equilibrium phase $P2_12_12_1$ appears, which had been reported by Prosandeev *et al.* with the property of interfering with ferroelectric anti-vortex and vortex in $BiFeO_3$ material.[60] It's a gyrotropic phase transition. When $-6.58\% < \eta < -6.01\%$ for CPI ($-7.45\% < \eta < -5.71\%$ for CSI), the stable state transforms from the original $P2_12_12_1$ state to the $P2_12_12$ state. When the η reaches to −6.58% and −7.45%, a phase transition from $P2_12_12$ to *Pc* phase has been obtained for CPI and CSI, respectively. Where, *Pc* state is much more stable with lower energy in the misfit strain range of $\eta < -6.58\%$ for CPI ($\eta < -7.45\%$ for CSI). So far as we know, no report involves *Pc* phase for other perovskites under the compressive strain region. It is important that the *Pc* state is a ferroelectric phase, containing the iodine octahedron and iodine quadrangular pyramid seen in Fig. S3.† Besides, the Fig. 1 also indicates that the axial ratio decreases gradually from 1.35 to 0.87 for CPI (1.36 to 0.88 for CSI).

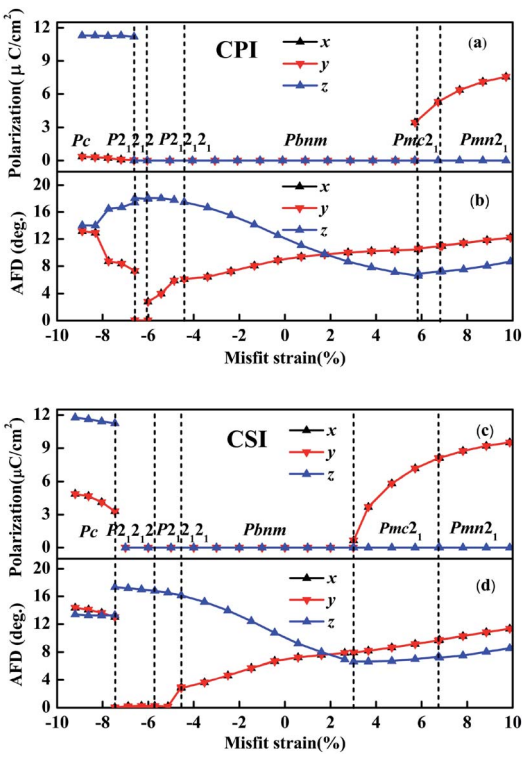

Fig. 2 The polarization and AFD *vs.* misfit strain in the [001] epitaxial CPI and CSI thin films, where *x*, *y*, and *z* axes is directed along pseudocubic [100], [010], and [001], respectively.

3.2 Antiferrodistortive vector and polarization

Antiferrodistortive (AFD) vector is an important measurement indicator to evaluate the deviate magnitude of iodine octahedron, which can be described by Cartesian components of the in-phase antiferrodistortive vector IAFD, and AAFD that of the antiphase antiferrodistortive vector. The $IAFD_z$ (out-of-plane component of the IAFD vector along *z* axis [001]) and $AAFD_{xy}$ (in-plane component of AAFD vector along *x* [100] or *y* [010] axis) of $CsMI_3$ (M = Pb, Sn) thin films in epitaxial (001) *vs.* the misfit stain are plotted in Fig. 2. Fig. 2 indicates that the $IAFD_z$ vector first decreases, and then increases gradually, while the $AAFD_{xy}$ vector increases gradually with the tensile strain increasing for CPI and CSI, respectively. Similarly one can see that the $IAFD_z$ vector first increases, and then decreases, whereas $AAFD_{xy}$ vector has the reverse tendency at all compressive strain regions. Apparently, whether CPI or CSI, the tendency is almost the same in each stable phase region, the deviate magnitude may exit small difference. Corresponding polarization directed along *x*, *y* and *z* axis can be estimated by the Berry phase method as plotted in Fig. 2. Simultaneously, in order to further verify the correctness of our calculation and understand the polar mechanism, we selected given misfit strain for each polar phase as an example by employing Born effective charges with the atomic displacements. In addition, the ground state structure *Pbnm* and the ferroelectric phase $Pmc2_1$ and $Pmn2_1$ are shown in Fig. 3 (*Pc* phase is shown in Fig. S4†). Firstly four layers alternate

array of $\sqrt{2} \times \sqrt{2} \times 2$ supercells of CPI and CSI have been used to decompose the polarization along the pseudocubic [001] direction as shown in Fig. 3. This decomposed polarization had been reported in $SrZrO_3$ to understand the polarization mechanism.[59] According to eqn (1) the decomposed polarization P_l can be obtained by

$$P_l = \frac{e}{V} \sum_{\alpha\beta}^{l} Z^{*i}_{\alpha\beta} \mu^{i}_{\beta} \quad (2)$$

where, $l = 1$, 2, 3 and 4 represent decomposed layers 1, 2, 3, 4 seen in Fig. 3(a), respectively. Correspondingly, the total polarization P can be decomposed P_1, P_2, P_3, and P_4. And i represents all the atoms in corresponding layer. V is the volume of the unit cell. Hence, we took centrosymmetric phase *P*4/*mmm* as reference phase of polarization phases *Pmc*2_1 and *Pmn*2_1, meanwhile, centrosymmetric phase *C*2/*m* is regarded as a reference phase of *Pc*. Three polarization phases have been decomposed into four layers as seen in Fig. 3 and S4.† Corresponding decomposed polar values given misfit strain are also presented in Fig. 3 and S4.† It's worth noting that layers 2 and 4 of *Pc* phase both miss one iodine atom due to its crystal structure contained the iodine quadrangular pyramid seen in Fig. S3 and S4.† To keep up with the number of atoms of layers 2 and 4 of the centrosymmetric phases *C*2/*m*, the missing atoms would be added in calculations.

Let us focus on *Pbnm* phase with misfit strain varying from −4.42% to 5.85% for CPI (−4.55% to 3.01% for CSI), *Pbnm* phase with an $a^-a^-c^+$ tilting pattern can be macroscopically described by an in-plane component of the $AAFD_{xy}$ as well as the out-of-plane component of the $IAFD_z$. $IAFD_z$ vector decreases gradually from 17.48° to 6.56° for CPI and from 16.14° to 6.65° for CSI. The tendency of $AAFD_{xy}$ is opposite to that of $IAFD_z$ varying from 6.09° to 10.47° for CPI (2.81° to 7.93° for CSI) as seen in Fig. 2. Even the degree of deviation of PbI_6 octahedron from normal PbI_6 octahedron is large, *Pbnm* phase is the paraelectric phase. The main reasons are (1) the polarization of each layer PbI_2 is zero, (2) the polarization of each layer CsI is not zero, but their polarization directions are opposite as seen in Fig. 3(b and f), (3) the total polarization of each type of atom in CPI (CSI) is always zero.

With the tensile strain increasing, two polarization phases *Pmc*2_1 and *Pmn*2_1 appear. Within the misfit strain range of their existence, their $AAFD_{xy}$ vector increase monotonically from 10.63° to 12.23° for CPI (8.17° to 11.35° for CSI) approximately, and their tendencies are similar to those of $IAFD_z$ vector. Fig. 2 further indicates *Pmc*2_1 possesses a polarization along in-plane (FE_{xy}). Hence, *Pmc*2_1 phase can be macroscopically described by an in-plane polarization FE_{xy} and the in-plane component of the $AAFD_{xy}$ as well as the out-of-plane component of the $IAFD_z$. Those macroscopical characters induced the mixing coupling modes FE_{xy} + $AAFD_{xy}$ and FE_{xy} + $IAFD_z$, which is different from the pure coupling of FE_{xy} + $AAFD_{xy}$ or FE_{xy} + $IAFD_z$ reported for *Pmc*2_1 phase in $SrZrO_3$ and $BiFeO_3$.[59,61,62] Of course, this mixing coupling mode had also been reported in $LaFeO_3$ and other

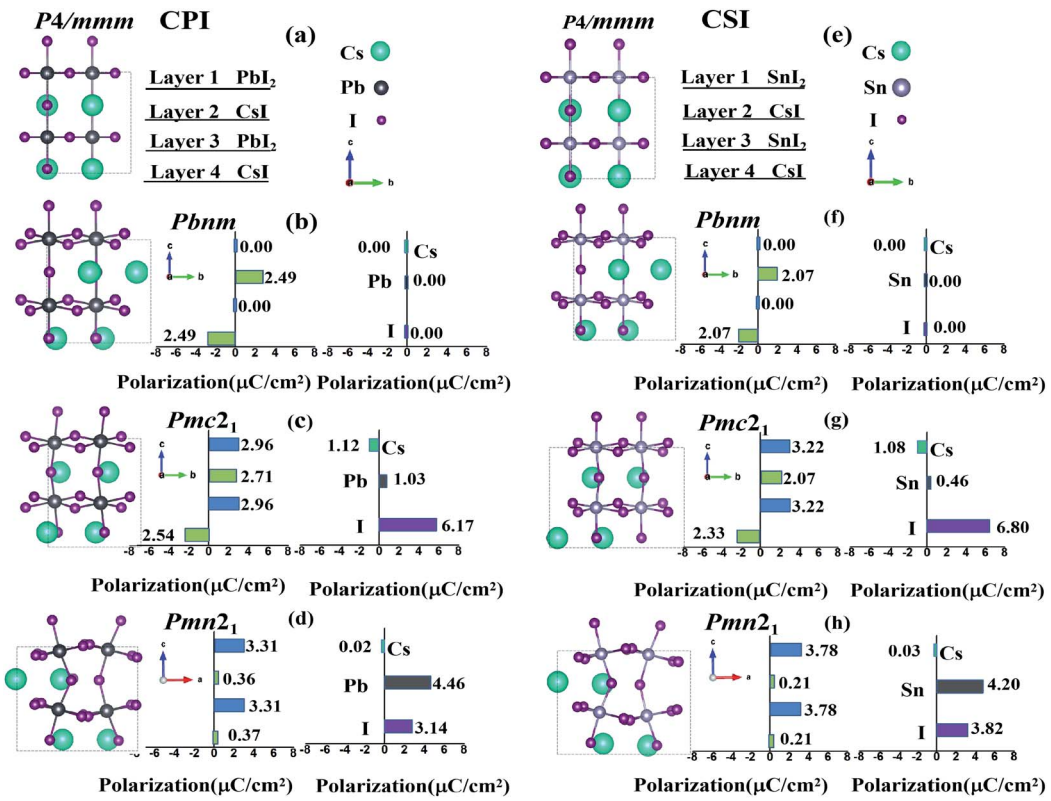

Fig. 3 The layer-decomposed polarization in corresponding strained phases for CPI and CSI. Panel (a) and (e) display the schematic configuration of the centrosymmetric *P*4/*mmm* structure. Panel (b), (c), (d), (f), (g) and (h) represent the layer-decomposed polarization in *Pbnm*, *Pmc*2_1, and *Pmn*2_1 phase, respectively.

rare-earth orthoferrites.[58,63] Moreover, from Fig. 2, as the misfit strain increases, the polarization FE_{xy} and antiferrodistortive $AAFD_{xy}$, $IAFD_z$ are all enhanced. Herein, Cs ions exit inverse displacements, which lead to an opposite polarization direction in two CsI layers, further weakening the total macroscopical polarization. Whether CPI or CSI, the major contributors to the total polarization come from I ions as shown in Fig. 3(c and g). Compared with $Pmc2_1$ phase, $Pmn2_1$ is also a ferroelectric phase with the same $a^-a^-c^+$ tilting pattern. Their difference is that (1) Cs ions exit homodromous displacements, and (2) the magnitude of polarization for CsI layer is very small compared to that of PbI_2 layer. (3) The main contribution to the total polarization derived from B-position cations (Pb or Sn).

In the compressive strain region, a fascinating polarization phase *Pc* is obtained, similar to *Pbnm*, $Pmc2_1$ and $Pmn2_1$ phases, *Pc* phase with $a^-a^-c^+$ tilting pattern can be described by in-plane component of the $AAFD_{xy}$ as well as out-of-plane component of the $IAFD_z$. Moreover, we also found that the $AAFD_{xy}$ vector tends to increase with the compressive stain varying from −6.58% to −10% for CPI, which is opposite to its $IAFD_z$ and similar to that of $P2_12_12$ and $P2_12_12_1$ phases. As is presented in Fig. 2, the corresponding polarization is estimated varying from 0.021 to 0.35 μC cm^{-2} along *xy* axis and from 11.20 to 11.30 μC cm^{-2} along *z* axis under corresponding compress strain region of $\eta < -6.58\%$ for CPI (3.30–4.86 μC cm^{-2} along *xy* axis and 11.25–11.76 μC cm^{-2} along *z* axis correspond to $\eta < -7.45\%$ for CSI) based on berry phase method, where *x*, *y*, and *z* are directed along pseudocubic [100], [010] and [001], respectively. Furthermore, compared with other polarization phases ($Pmc2_1$ and $Pmn2_1$), the polarization of *Pc* phase is not only directed along *xy* axis, but also along *z* axis, which may be attributed to the crystal structure composed of iodine octahedron and iodine quadrangular pyramid. Noted that, similar to the $Pmn2_1$ phase, the polarization comes mainly from B-position cations (Pb or Sn).

3.3 Electronic properties

Based on those stable phases, we search the suitable band gap to photovoltaic materials, the band gaps of $CsMI_3$ (M = Pb, Sn) are estimated based on PBEsol functional under different misfit strains as plotted in Fig. 4. Fig. 4 indicates that the band gap of the material can be adjusted by the epitaxial strain. And tendencies of band gap for $CsMI_3$ (M = Pb, Sn) are approximately the same as that of strain. Besides, from Fig. 4(a) we found that the band gap values of *Pbnm*, $P2_12_12_1$, and $P2_12_12$ states for CPI are from 1.14 eV to 1.58 eV, which are beneficial candidates of photovoltaic materials. We also found the tendencies of the band gap under compressive and tensile strain are different for *Pbnm* phase. The band gap value of the *Pbnm* state decreases monotonically under compressive strain from 1.58 eV to 1.18 eV for CPI and from 0.42 eV to nearly zero eV for CSI, but from 1.58 eV to 1.55 eV for CPI and from 0.42 eV to 0.47 eV for CSI under tensile strain. Differently, except *Pbnm* phase, whether the compressive strain or tensile strain, the tendency of band gaps increases monotonically for $CsMI_3$ (M = Pb, Sn).

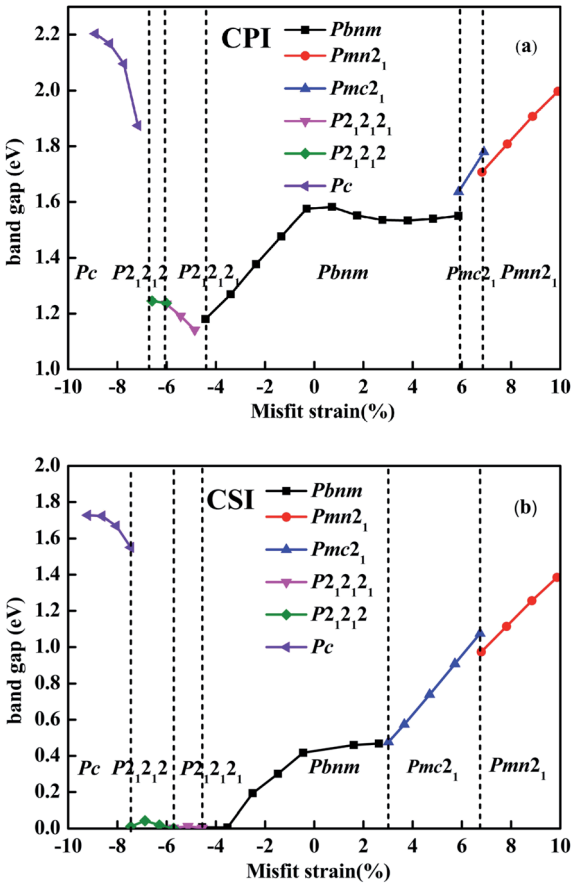

Fig. 4 Band gaps of different stable phases *vs.* misfit strain of CPI and CSI, respectively.

A noteworthy feature of electronic properties in *Pbnm* state is the diminution of band gap with the increasing of compressive strain, corresponding to the nearly unchanged band gap under tensile strain. Particularly, the unusual electronic properties are not associated with structural phase transition as we commonly expected, which are demonstrated by the same structural symmetry (*i.e.*, *Pbnm*) and the linear changes of bond angles and bond lengths (as shown in Fig. S5†). In order to better understand the origin of the unusual electronic properties, we calculate the band structure and density of states, as well as the corresponding charge density at *G* point of the conduction-band minimum of *Pbnm* state for CPI film with strains of −3.39% and 1.74%, respectively. Note that the conduction-band minimum is dominated by Pb-p*x* orbital under tensile strain, while that is dominated by Pb-p*z* orbital under compressive strain, as shown in Fig. 5. In other words, the compressive strain lows the energy of antibonding Pb-p*z* orbital, which results in the rapid shift of the corresponding conduction band towards the valence-band maximum and the occupation of conduction-band minimum. As a result, the band gap rapidly decreases when the compressive strain increases. Such striking electronic properties hint towards unusual optical properties—such as electric dipole transition and piezochromic effects.[64–66] In fact, we numerically found (see Fig. 4(b)) that such feature also exists in $CsSnI_3$ film but the band gap changes from 0.42 eV to 0 eV

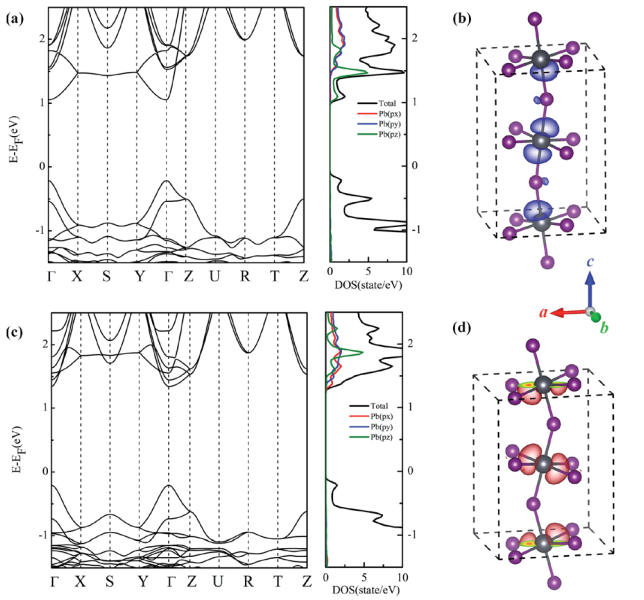

Fig. 5 The calculated (a) band structure and density of states, as well as (b) the corresponding charge density at Γ point of the conduction-band minimum of *Pbnm* state with strains of −3.39%, respectively. Panels (c) and (d): the same as in panels (a) and (b), respectively, but for 1.74% strain in CPI film.

with strain-induced insulator-to-metal transitions under −3.8% compressive strain, which further emphasizes the significance.

4 Conclusions

The first-principles calculations are carried out to explore the structural phase transition, electric polarization and electric properties of $CsMI_3$ (M = Pb, Sn) epitaxial films along (001) direction. Taken the strain effect into account, the phase diagrams of $CsMI_3$ (M = Pb, Sn) epitaxial films have been presented, which exhibits three ferroelectric phases $Pmc2_1$, $Pmn2_1$, *Pc* and two paraelectric phases $P2_12_12_1$, $P2_12_12$. The difference is that the misfit strain of the same phase transition is different in two phase diagrams. Surprisingly, a ferroelectric phase *Pc* and a paraelectric phase $P2_12_12_1$ with gyrotropic phase transitions are found in two photovoltaic materials. By comparison, the magnitudes of antiferrodistortive vector and electric polarization of $CsPbI_3$ epitaxial films are always smaller than that of in $CsSnI_3$ epitaxial films under given misfit stain, which may be attributed to the fact that it's easier to deviate from the corresponding center symmetric position for Sn ions with the small atomic radius compared to Pb ions. Unusual electronic properties in *Pbnm* state under epitaxial strains are also revealed to be directly related to the strain effect on electric structure, as, *e.g.*, evidenced by the rapid shift of pz conduction band towards the valence-band maximum and the occupation of conduction-band minimum, without structural phase transition as we commonly expected. We thus hope that the present work broadens the general and important fields of, *e.g.*, phase transitions in films, and will encourage scientists to observe such unusual effects in all-inorganic halides as well as in other compounds.

Conflicts of interest

There are no conflicts to declare.

Acknowledgements

This work was supported by the National Natural Science Foundation of China (No. 11574220 and 11874043). H. T. is thankful for the support of the China Postdoctoral Science Foundation (No. 2018M642205) and the Jiangsu Planned Projects for Postdoctoral Research Funds (No. 2019K249).

References

1 Y. El Ajjouri, F. Locardi, M. C. Gélvez-Rueda, M. Prato, M. Sessolo, M. Ferretti, F. C. Grozema, F. Palazon and H. J. Bolink, *Energy Technol.*, 2019, 1900788.
2 D.-J. Yang, Y.-H. Du, Y.-Q. Zhao, Z.-L. Yu and M.-Q. Cai, *Phys. Status Solidi B*, 2019, 1800540.
3 B. Zhao, S.-F. Jin, S. Huang, N. Liu, J.-Y. Ma, D.-J. Xue, Q. Han, J. Ding, Q.-Q. Ge, Y. Feng, *et al.*, *J. Am. Chem. Soc.*, 2018, **140**, 11716–11725.
4 J. Bisquert, *J. Phys. Chem. Lett.*, 2013, **4**, 2579–2598.
5 N.-G. Park, *J. Phys. Chem. Lett.*, 2013, **4**, 2423–2429.
6 A. Kojima, K. Teshima, Y. Shirai and T. Miyasaka, *J. Am. Chem. Soc.*, 2009, **131**, 6050–6051.
7 S. Zhang, X. Yang, Y. Numata and L. Han, *Energy Environ. Sci.*, 2013, **6**, 1443–1464.
8 M. M. Lee, J. Teuscher, T. Miyasaka, T. N. Murakami and H. J. Snaith, *Science*, 2012, **338**, 643–647.
9 A. S. Thind, X. Huang, J. Sun and R. Mishra, *Chem. Mater.*, 2017, **29**, 6003–6011.
10 R. J. Sutton, G. E. Eperon, L. Miranda, E. S. Parrott, B. A. Kamino, J. B. Patel, M. T. Hörantner, M. B. Johnston, A. A. Haghighirad, D. T. Moore, *et al.*, *Adv. Energy Mater.*, 2016, **6**, 1502458.
11 Y. Hu, F. Bai, X. Liu, Q. Ji, X. Miao, T. Qiu and S. Zhang, *ACS Energy Lett.*, 2017, **2**, 2219–2227.
12 J. K. Nam, S. U. Chai, W. Cha, Y. J. Choi, W. Kim, M. S. Jung, J. Kwon, D. Kim and J. H. Park, *Nano Lett.*, 2017, **17**, 2028–2033.
13 Y. Chen, J. Barnard, R. Palmer, M. Watanabe and T. Sasaki, *Phys. Rev. Lett.*, 1999, **83**, 2406.
14 W. Shockley and H. J. Queisser, *J. Appl. Phys.*, 1961, **32**, 510–519.
15 C. Yu, Y. Ren, Z. Chen and K. Shum, *J. Appl. Phys.*, 2013, **114**, 163505.
16 K. Shum, Z. Chen, J. Qureshi, C. Yu, J. J. Wang, W. Pfenninger, N. Vockic, J. Midgley and J. T. Kenney, *Appl. Phys. Lett.*, 2010, **96**, 221903.
17 Z. Chen, C. Yu, K. Shum, J. J. Wang, W. Pfenninger, N. Vockic, J. Midgley and J. T. Kenney, *J. Lumin.*, 2012, **132**, 345–349.
18 E. L. Da Silva, J. M. Skelton, S. C. Parker and A. Walsh, *Phys. Rev. B: Condens. Matter Mater. Phys.*, 2015, **91**, 144107.
19 E. M. Sanehira, A. R. Marshall, J. A. Christians, S. P. Harvey, P. N. Ciesielski, L. M. Wheeler, P. Schulz, L. Y. Lin, M. C. Beard and J. M. Luther, *Sci. Adv.*, 2017, **3**, eaao4204.
20 K. Marshall, M. Walker, R. Walton and R. Hatton, *Nature Energy*, 2016, **1**, 16178.

21 K. Yamada, S. Funabiki, H. Horimoto, T. Matsui, T. Okuda and S. Ichiba, *Chem. Lett.*, 1991, **20**, 801–804.
22 S. Xiang, Z. Fu, W. Li, Y. Wei, J. Liu, H. Liu, L. Zhu, R. Zhang and H. Chen, *ACS Energy Lett.*, 2018, **3**, 1824–1831.
23 J. Pan, Y. Shang, J. Yin, M. De Bastiani, W. Peng, I. Dursun, L. Sinatra, A. M. El-Zohry, M. N. Hedhili, A.-H. Emwas, *et al.*, *J. Am. Chem. Soc.*, 2017, **140**, 562–565.
24 Q. Wang, X. Zheng, Y. Deng, J. Zhao, Z. Chen and J. Huang, *Joule*, 2017, **1**, 371–382.
25 R. J. Sutton, M. R. Filip, A. A. Haghighirad, N. Sakai, B. Wenger, F. Giustino and H. J. Snaith, *ACS Energy Lett.*, 2018, **3**, 1787–1794.
26 P. Xu, S. Chen, H.-J. Xiang, X.-G. Gong and S.-H. Wei, *Chem. Mater.*, 2014, **26**, 6068–6072.
27 S. M. Young and A. M. Rappe, *Phys. Rev. Lett.*, 2012, **109**, 116601.
28 I. Chung, J.-H. Song, J. Im, J. Androulakis, C. D. Malliakas, H. Li, A. J. Freeman, J. T. Kenney and M. G. Kanatzidis, *J. Am. Chem. Soc.*, 2012, **134**, 8579–8587.
29 M. Han, J. Sun, M. Peng, N. Han, Z. Chen, D. Liu, Y. Guo, S. Zhao, C. Shan, T. Xu, *et al.*, *J. Phys. Chem. C*, 2019, **123**, 17566–17573.
30 J. S. Han, Q. V. Le, J. Choi, H. Kim, S. G. Kim, K. Hong, C. W. Moon, T. L. Kim, S. Y. Kim and H. W. Jang, *ACS Appl. Mater. Interfaces*, 2019, **11**, 8155–8163.
31 J. Chen, Z. Luo, Y. Fu, X. Wang, K. J. Czech, S. Shen, L. Guo, J. C. Wright, A. Pan and S. Jin, *ACS Energy Lett.*, 2019, **4**, 1045–1052.
32 S. Ma, S. H. Kim, B. Jeong, H.-C. Kwon, S.-C. Yun, G. Jang, H. Yang, C. Park, D. Lee and J. Moon, *Small*, 2019, **15**, 1900219.
33 J. B. Hoffman, A. L. Schleper and P. V. Kamat, *J. Am. Chem. Soc.*, 2016, **138**, 8603–8611.
34 A. Waleed, M. M. Tavakoli, L. Gu, S. Hussain, D. Zhang, S. Poddar, Z. Wang, R. Zhang and Z. Fan, *Nano Lett.*, 2017, **17**, 4951–4957.
35 A. Swarnkar, W. J. Mir and A. Nag, *ACS Energy Lett.*, 2018, **3**, 286–289.
36 G. E. Eperon, G. M. Paterno, R. J. Sutton, A. Zampetti, A. A. Haghighirad, F. Cacialli and H. J. Snaith, *J. Mater. Chem. A*, 2015, **3**, 19688–19695.
37 A. Swarnkar, A. R. Marshall, E. M. Sanehira, B. D. Chernomordik, D. T. Moore, J. A. Christians, T. Chakrabarti and J. M. Luther, *Science*, 2016, **354**, 92–95.
38 T. Zhang, M. I. Dar, G. Li, F. Xu, N. Guo, M. Grätzel and Y. Zhao, *Sci. Adv.*, 2017, **3**, e1700841.
39 P. Luo, W. Xia, S. Zhou, L. Sun, J. Cheng, C. Xu and Y. Lu, *J. Phys. Chem. Lett.*, 2016, **7**, 3603–3608.
40 S. Yang, J. Seidel, S. Byrnes, P. Shafer, C.-H. Yang, M. Rossell, P. Yu, Y.-H. Chu, J. Scott, J. Ager III, *et al.*, *Nat. Nanotechnol.*, 2010, **5**, 143.
41 R. Guo, L. You, Y. Zhou, Z. S. Lim, X. Zou, L. Chen, R. Ramesh and J. Wang, *Nat. Commun.*, 2013, **4**, 1990.
42 L.-y. Huang and W. R. Lambrecht, *Phys. Rev. B: Condens. Matter Mater. Phys.*, 2013, **88**, 165203.
43 T. Choi, S. Lee, Y. J. Choi, V. Kiryukhin and S.-W. Cheong, *Science*, 2009, **324**, 63–66.
44 J. Seidel, D. Fu, S.-Y. Yang, E. Alarcón-Lladó, J. Wu, R. Ramesh and J. W. Ager III, *Phys. Rev. Lett.*, 2011, **107**, 126805.
45 X. Wang, S. Zhen, Y. Min, P. Zhou, Y. Huang, C. Zhong, Z. Dong and J. Liu, *J. Appl. Phys.*, 2017, **122**, 194102.
46 Y. Li, X. Gong, P. Zhang and X. Shao, *Chem. Phys. Lett.*, 2019, **716**, 76–82.
47 Y. Huang, Z. Hu, K. Li and X. Shao, *Comput. Mater. Sci.*, 2018, **143**, 403–410.
48 G. Kresse and D. Joubert, *Phys. Rev. B: Condens. Matter Mater. Phys.*, 1999, **59**, 1758.
49 J. P. Perdew, A. Ruzsinszky, G. I. Csonka, O. A. Vydrov, G. E. Scuseria, L. A. Constantin, X. Zhou and K. Burke, *Phys. Rev. Lett.*, 2008, **100**, 136406.
50 J. P. Perdew, K. Burke and M. Ernzerhof, *Phys. Rev. Lett.*, 1996, **77**, 3865.
51 R. King-Smith and D. Vanderbilt, *Phys. Rev. B: Condens. Matter Mater. Phys.*, 1994, **49**, 5828.
52 R. Resta, M. Posternak and A. Baldereschi, *Phys. Rev. Lett.*, 1993, **70**, 1010.
53 H. T. Stokes and D. M. Hatch, *J. Appl. Crystallogr.*, 2005, **38**, 237–238.
54 K. Momma and F. Izumi, *J. Appl. Crystallogr.*, 2011, **44**, 1272–1276.
55 S. Baroni, S. De Gironcoli, A. Dal Corso and P. Giannozzi, *Rev. Mod. Phys.*, 2001, **73**, 515.
56 K. Refson, P. R. Tulip and S. J. Clark, *Phys. Rev. B: Condens. Matter Mater. Phys.*, 2006, **73**, 155114.
57 G. Song, B. Gao, G. Li and J. Zhang, *RSC Adv.*, 2017, **7**, 41077–41083.
58 A. Mao, H. Tian, X. Kuang, J. Jia and J. Chai, *RSC Adv.*, 2016, **6**, 100526–100531.
59 H. Tian, A.-J. Mao, H. J. Zhao, Y. Cui, H. Li and X.-Y. Kuang, *Phys. Chem. Chem. Phys.*, 2016, **18**, 7680–7687.
60 S. Prosandeev, I. A. Kornev and L. Bellaiche, *Phys. Rev. Lett.*, 2011, **107**, 117602.
61 Y. Yang, W. Ren, M. Stengel, X. Yan and L. Bellaiche, *Phys. Rev. Lett.*, 2012, **109**, 057602.
62 S. Prosandeev, D. Wang, W. Ren, J. Íñiguez and L. Bellaiche, *Adv. Funct. Mater.*, 2013, **23**, 234–240.
63 H. J. Zhao, Y. Yang, W. Ren, A.-J. Mao, X. M. Chen and L. Bellaiche, *J. Phys.: Condens. Matter*, 2014, **26**, 472201.
64 W. Meng, X. Wang, Z. Xiao, J. Wang, D. B. Mitzi and Y. Yan, *J. Phys. Chem. Lett.*, 2017, **8**, 2999–3007.
65 H. Tian, X.-Y. Kuang, A.-J. Mao, Y. Yang, C. Xu, S. O. Sayedaghaee and L. Bellaiche, *Phys. Rev. B*, 2018, **97**, 020103.
66 D. Sando, Y. Yang, E. Bousquet, C. Carrétéro, V. Garcia, S. Fusil, D. Dolfi, A. Barthélémy, P. Ghosez, L. Bellaiche, *et al.*, *Nat. Commun.*, 2016, **7**, 10718.

